

Flow tagging velocimetry using caged dye photo-activated fluorophores

Walter R Lempert[†] and Scott R Harris[‡]

[†] Departments of Mechanical Engineering and Chemistry, The Ohio State University, Columbus, OH 43210, USA

[‡] Multifunction EO Sensors Branch, Air Force Research Laboratory/SNJM, Wright Patterson AFB, OH 45433-7700, USA

Received 13 January 2000, in final form and accepted for publication 27 April 2000

Abstract. The use of caged dye photo-activated fluorophore velocimetry is described and representative examples are presented. After a brief survey of recently reported measurements, a more detailed example of the flow produced in a cylinder with a single rotating end wall is presented. Simultaneous stereoscopic image sets in the (r, z) and (r, θ) planes have been obtained over a Reynolds number range of roughly 10^2 – 10^5 . At low Reynolds numbers (≈ 0 – 2000), the steady, axisymmetrical flow is found to quantitatively agree with predictions from a numerical flow solver. At higher Reynolds numbers (from 5×10^3 to 10^5), the flow develops considerable turbulent three-dimensional structure.

Keywords: flow tagging velocimetry, photo-activated fluorophores, rotating flows, vortex breakdown

1. Introduction

Recent advances in laser and optical technology have motivated the development of new quantitative velocimetry techniques based on two- (and three-) dimensional laser induced fluorescence (LIF) imaging. In general, these techniques can be broadly classified as either ‘Doppler’ or ‘time-of-flight’. Unlike scattering based approaches, such as laser Doppler velocimetry, Doppler based LIF techniques most commonly utilize the spectral shift of resonant atomic or molecular absorption features that are associated with the component of fluid motion parallel to the direction of a propagating laser sheet. Since such features are typically somewhat spectrally broad (of order 1 GHz), reported Doppler-shifted LIF measurements have mostly been confined to high speed flows (Zimmerman and Miles 1980, McDaniel 1983, Paul *et al* 1989).

Fluorescence time-of-flight techniques determine velocity by imaging the displacement elapsed during a well defined time interval. Since, in principle, the time interval can be made arbitrarily long, time-of-flight techniques are more suited to measuring low to moderate velocities, such as those typical of incompressible flows. This paper will focus on what has been termed caged dye photo-activated fluorophore (PAF) flow tagging velocimetry. Flow tagging refers to a class of time-of-flight techniques in which a laser beam is used to ‘write’ a pattern into a flow by means of a suitable optical excitation. After an appropriate time delay, during which time the original pattern is advected by the flow, the new position is ‘interrogated’ using planar laser induced fluorescence (PLIF) sheet imaging. Flow tagging based on vibrational excitation of molecular oxygen, which has been termed

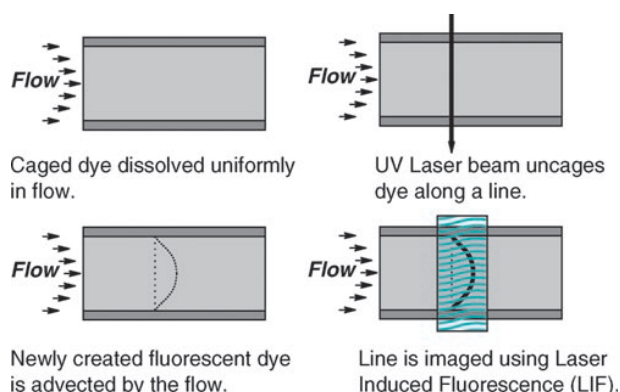


Figure 1. A schematic illustration of the use of caged dye PAFs for flow tagging velocimetry.

Raman excitation followed by laser induced electronic fluorescence, has been applied both to low speed turbulent air jets (Noulez *et al* 1997) and to supersonic flow (Miles *et al* 1989). Gas phase flow tagging based on *in situ* laser production of hydroxyl radicals (Boedeker 1989, Goss *et al* 1991) and, more recently, ozone (Ribarov *et al* 1999) has also been reported. An inverse type of tagging, in which a two-colour, multi-photon absorption is used to photo-bleach sodium that is seeded into a flow, has also been reported recently (Barker *et al* 1997).

We have introduced the use of caged dye PAFs as flow tagging tracers in water and alcohol flows (Lempert *et al* 1995, 1998). PAFs are nominally fluorescent dyes that have been rendered nonfluorescent by strategic attachment of a chemical ‘caging’ group. The chemical caging group is

photolytically cleaved upon absorption of a single photon of ultraviolet light. After photolysis, the fluorescent dye is recovered and can be tracked indefinitely using ordinary laser induced fluorescence imaging techniques. In effect, as illustrated in figure 1, the tagging laser is used to photochemically create a user defined pattern of fluorescent dye. The convection of the 'locally seeded' fluid elements is subsequently interrogated using a second laser. In all work reported to date, the tagging has been performed using the third harmonic of an Nd:YAG laser at 355 nm. Interrogation has utilized visible lasers, most commonly argon-ion lasers, flashlamp-pumped dye lasers, or the second harmonic of Nd:YAG (continuous wave or pulsed).

It should be pointed out that the PAF velocimetry technique is similar, in many respects, to the photochromic tracer technique (Popovich and Hummel 1967) and to what has been referred to as either laser-induced photochemical anemometry (Falco and Nocera 1993) or molecular tagging velocimetry (Gendrich *et al* 1997, Koochesfahani *et al* 1996).

2. Experimental considerations

The majority of measurements performed to date using PAF dyes have employed some form of caged fluorescein. With the exception of the addition of a carboxy dextran group of variable relative molecular mass and one (or more) 'caging' groups, the chemical structure of the uncaged form is identical to that of ordinary fluorescein dye. Absorption of a single UV photon results in *permanent* photolytic cleavage of the caging groups. Owing to its high brightness and fortuitous spectral overlap with the argon-ion laser, fluorescein dye has commonly been employed for passive scalar mixing and flow visualization studies (Koochesfahani and Dimotakis 1985, 1986, Dahm and Dimotakis 1990). Like fluorescein, the uncaged PAF dye has a fairly broad (≈ 30 nm), strong absorption band centred at 480 nm (blue) and exhibits intense fluorescence emission (quantum yield ≈ 0.90) centred at 550 nm (green). More recently (Lempert *et al* 1998), caged rhodamine PAFs with optical properties similar to those of caged fluorescein, but with their optical absorption shifted to ≈ 530 nm, have been developed. Caged rhodamine PAFs are well suited to interrogation using the second harmonic of a Nd:YAG laser at 532 nm.

The principal advantage of caged dye PAF tracers is that they exhibit very strong fluorescence. As discussed in more detail by Lempert (2000), the radiative decay of the upper electronic state is sufficiently fast (of order a few nanoseconds) that many photons (10^2 – 10^8 or more, depending on the interrogation source) can be extracted from each uncaged dye molecule during a single interrogation. Additionally, since the tagging is permanent, PAFs can be used for measurements in exceedingly slow flows. For example, as will be illustrated in section 3, Harris *et al* (1996), has reported quantitative measurements in electrohydrodynamic flows with mean velocities of order 2 – $4 \mu\text{m s}^{-1}$.

There are, however, some significant disadvantages associated with caged dye tracers. Fundamentally, the most significant is the finite kinetic rate of the photochemical cage breaking step. This has been described in some detail

previously (Lempert *et al* 1995, 1998) and has the effect of imposing a minimum delay time between tagging and interrogation. To date, the minimum delay time which has been reported in caged dye PAF studies is $200 \mu\text{s}$ (Lempert *et al* 1995). This corresponds to $\approx 5\%$ of the kinetic $1/e$ rise time of the fluorescence signal. The second principal disadvantage of caged dye PAFs is that the materials can be used once only, since the uncaging is irreversible. This is compounded by the high cost of the tracer itself. PAFs were originally developed by the biological sciences community for cell-related studies which typically require exceedingly small (of order a milligram) quantities of tracer. The high brightness of the uncaged dye results in very modest ($\approx 1 \text{ mg l}^{-1}$) concentration requirements, but the cost can still be prohibitive. A variety of caged dye PAFs is available commercially from Molecular Probes, Inc (Eugene, Oregon, USA).

3. A survey of recent measurements employing caged dye PAFs

Caged dye tracers have been employed in a wide variety of flow problems, with characteristic velocities ranging from the order of micrometres to metres per second and characteristic length scales ranging from 0.10 mm to 1.0 m. In this section we give a very brief survey of measurements which have been reported to date, with emphasis on providing examples of the applicability of the diagnostic to a range of fluid applications. More detail can be found in the references cited.

At the low end of the length scale, Paul *et al* (1998) have obtained quantitative velocity contours in pressure and electrokinetically driven flow through open capillaries of order $100 \mu\text{m}$ diameter. For a typical pressure driven case, at a Reynolds number of 0.034, a classic parabolic profile was obtained with a centreline velocity of $450 \mu\text{m s}^{-1}$. Quantitative velocity data were obtained by recording a pair of interrogation images, separated by 20 ms, and using the scalar imaging velocimetry (SIV) inversion technique developed by Dahm *et al* (1992). The spatial resolution reported was approximately $5 \mu\text{m}$. In the case of electrokinetically driven flow, it was noted that the extraction of quantitative data is complicated by the fact that caged fluorescein is charged in solution. Separation of the drift velocity of the charged tracer from the true fluid convective velocity was found to be a considerable problem. The authors also noted a systematic error in data obtained near the capillary wall, which also was attributed to possible charge effects.

Several studies of internal circulation in droplets have been reported. Figure 2(a) shows a tag/interrogate image pair obtained from a free falling water droplet (Harris *et al* 1996). The image on the left-hand side of figure 2(a) is due to elastic scattering from a single tagging pulse. The image on the right-hand side of figure 2(a) shows the interrogated line segment 29.5 ms later. The droplet in figure 2 is approximately 5 mm in diameter and was formed from a common laboratory burette that was gravity fed from a reservoir containing a 0.20 mg l^{-1} ($6.7 \times 10^{-8} \text{ M}$) solution of caged fluorescein of molecular mass 3000. As described in the next section, quantitative measurement of internal

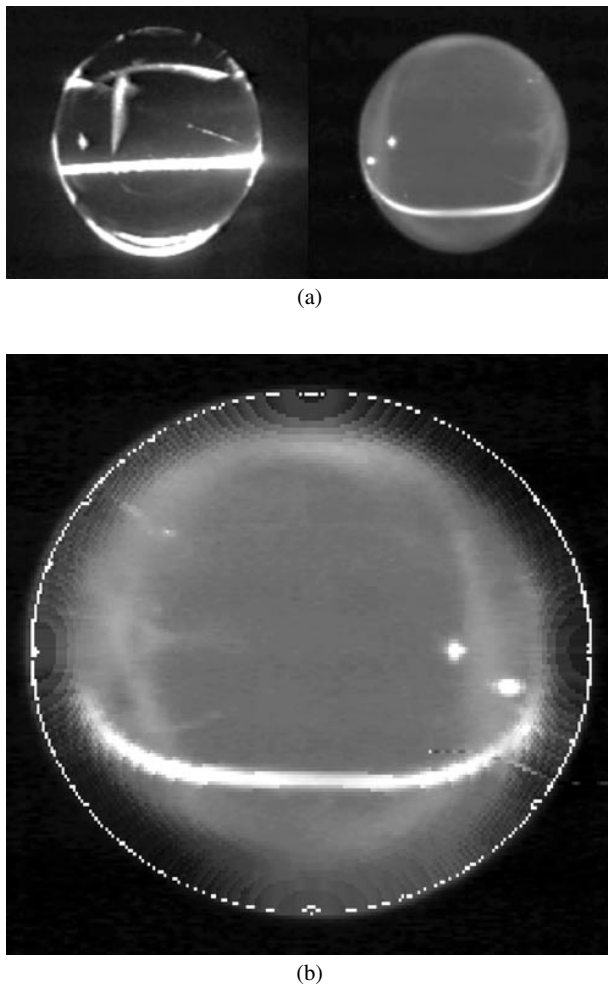


Figure 2. (a) Tag (left-hand image) and interrogate (right-hand image) raw image pair obtained from a free falling water droplet using caged fluorescein PAF. The time delay is 29.5 ms. (b) The result of applying ray tracing corrections to the right-hand image in (a) (from Harris *et al* (1996)).

circulation requires that the raw images be corrected for the influence of droplet curvature. In effect, the droplet/air interface acts as a spherical lens, introducing significant distortion. Several techniques for removing this optical distortion have been reported, including rather sophisticated approaches which remove both geometrical and intensity distortion (Zhang and Melton 1994). Application of a simple ray-tracing procedure (Harris *et al* 1996), summarized in the next section, gives the image shown in figure 2(b). It can be seen that the region very close to the droplet edge is obscured by total internal reflection. Less obviously, the magnitude (and in some cases the sign) of the measured velocity is greatly effected. Harris *et al* (1996) report corrections of up to 100%. Similar data have been obtained for alcohol droplets (Lempert *et al* 1998) using a caged rhodamine dye. In this case, evaporation of alcohol was found to induce exceedingly complex internal flow patterns.

As an example of an exceedingly low flow velocity, a time sequence of images from a model electrohydrodynamic flow known as a Taylor cone has been obtained (Vizka and Saville 1992). The cone is formed by immersing a pair of electrodes in silicon oil, upon the bottom of which is placed

a water droplet. The semispherical droplet is 'stretched' into a cone by application of an approximately 2 kV cm^{-1} field. The fluid velocity reported was in the range approximately $2\text{--}4 \mu\text{m s}^{-1}$.

As an example of a physically larger and higher Reynolds number flow field, Biage *et al* (1996) obtained a large data set of images from the flow produced between rotating concentric cylinders (Taylor–Couette flow). The cylinder height was 102 cm and the inner and outer cylinder radii were 3.14 and 8.18 cm, respectively. Sets of images were obtained over a Reynolds number range, given by the inner/outer cylinder gap spacing, between 154 and 3.5×10^5 and were used to obtain instantaneous velocity profiles and spectral density functions.

As a second example of measurement in turbulent flow, Guilkey *et al* (1996) utilized caged dyes to study scalar mixing in a turbulent pipe at a Reynolds number of 7500. In these experiments, a cylindrical optical system was used to create a spatial 'square-wave' pattern of uncaged dye. The temporal evolution of this initial pattern was subsequently monitored at several downstream locations. It was found that the initial square-wave pattern decayed rapidly, becoming dominated by higher frequency components at values of X/D equal to approximately 50. At $X/D = 71$, a long wavelength component appeared, as predicted in previous theoretical work by some of the same authors (Kerstein and McMurty 1994).

As a final example, Dussaud *et al* (1998) utilized caged dyes to visualize the spreading of involatile and volatile surface films on water. In both cases, images were obtained by writing a pair of vertical lines into a 16 cm diameter tank filled with a solution of caged fluorescein. A single droplet of solvent was then deposited onto the quiescent surface. Surface tension causes the droplet to rapidly spread into a thin surface film. The sublayer flow pattern induced during the spreading was captured by viewing the interrogated image from the side. For the involatile fluid (silicon oil), the experimental velocity data agreed well with Blasius model predictions for a laminar boundary layer. For a volatile fluid (*p*-xylene) the sublayer flow was highly rotational, which the authors attributed to the onset of a thermal instability induced by evaporation.

4. Rotating end wall flow, a representative example

4.1. Background

In this section we use the representative example of the flow produced in a cylinder with a single rotating end wall to provide a more detailed look at caged dye flow tagging. This flow is attractive because it provides a relatively simple model system for the study of what is known as vortex breakdown. Although a precise definition is somewhat elusive, vortex breakdown is generally characterized by the formation of a stagnation point, followed by a swelling (or 'bursting') of the vortex and the creation of a region of recirculation. After Vogel's initial observation of vortex breakdown in this flow (Vogel 1975), Escudier (1984) utilized fluorescent dye visualization to systematically explore the flow over a wide range of the parameter space. Recent numerical

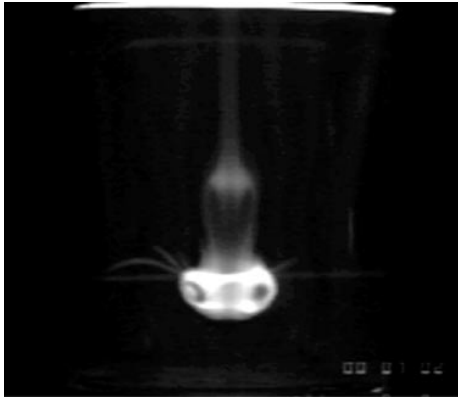


Figure 5. An interrogated image of lid driven cylinder flow at $Re = 1890$ and $\delta = 2.0$. Tagging is at same position as in figure 4. Flow was tagged several times and then allowed to evolve for several minutes prior to interrogation.

breakdown bubble zones. As the Reynolds number is further increased (to $Re \simeq 3000$), the flow becomes unsteady, while maintaining axisymmetry. As will be illustrated in the next section, at even higher Reynolds number ($Re \simeq 3500$), the flow becomes three dimensional, including significant turbulent fluctuations in the boundary layer.

4.4. Quantitative studies on steady flow

Extraction of quantitative velocity data from flow tagging images requires the consideration of several issues, the most important of which is the ambiguity associated with motion parallel to the direction of the line. This has been discussed in some detail by several authors (Hill and Klewicki 1996, Koochesfahani *et al* 1996, Paul *et al* 1998, Harris *et al* 1996) and has resulted in several strategies which will only be summarized here. The simplest approach is to employ the minimum possible time delay, Δt , between tagging and interrogation, since the uncertainty in the displaced line position, E , is given by

$$E = \left(\frac{\partial w}{\partial x} \right) u \Delta t^2 \quad (1)$$

where w is the component of velocity perpendicular to the tagged line (typically the principal flow axis) and u is the velocity component parallel to the line. Clearly, minimizing Δt minimizes this contribution to the displacement uncertainty. The finite spatial resolution of cameras, however, causes the displacement uncertainty to increase with decreasing Δt . The use of this approach, therefore, involves an inherent trade-off and often is not a satisfactory solution. A second approach is to form a more extensive grid pattern, utilizing the crossing points for unambiguous two-component velocity determination. This has been described extensively by Koochesfahani and co-workers (Gendrich and Koochesfahani 1996, Gendrich *et al* 1997, Koochesfahani *et al* 1996). A third approach is to capture a sequence of images and employ the SIV data inversion procedure. This, as mentioned previously, is described in detail by Dahm *et al* (1992) and has been employed by Paul *et al* (1998).

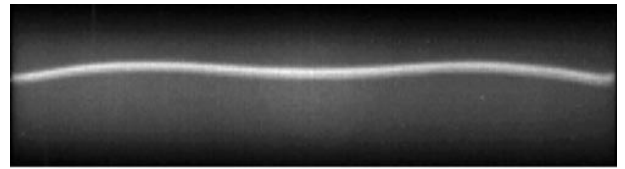


Figure 6. An interrogated image of the vertical component of displacement in lid driven cylinder flow at $Re = 1410$ and $\delta = 2.0$.

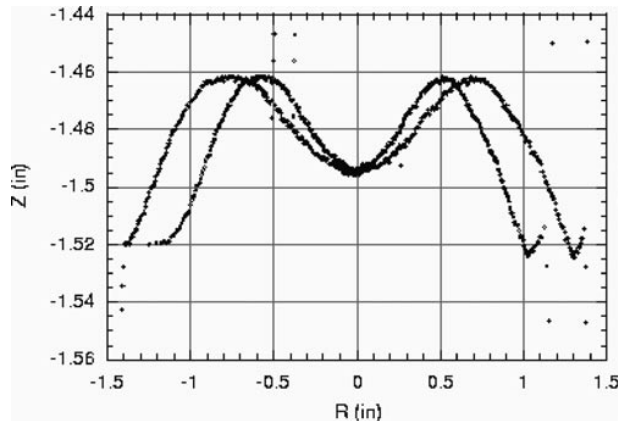


Figure 7. A comparison of uncorrected (+) and corrected, ray traced (\diamond) displacements obtained from image data of figure 6.

A final approach, applicable to regimes amenable to direct numerical simulation and which was adopted in this portion of the present work, is direct Lagrangian frame comparison of the observed displacement with computational prediction. This is achieved by ‘writing’ a line into the computation and allowing it to evolve in a series of real-time steps. As an example, figure 6 shows a representative image obtained from the side viewing camera at a Reynolds number of 1410 and $\delta = 2.0$. The line was tagged across the diameter at a non-dimensionalized vertical position equal to $1.15R$, measured from the rotating lid. The time between tagging and interrogation was 0.40 s.

The displacement at each lateral pixel location along the line is extracted from the image using a standard least-squares fitting procedure (Bevington 1969). The greyscale intensity distribution perpendicular to the line is modelled as a Gaussian, corresponding to the idealized tagging laser intensity distribution, superimposed on a linear background. With this approach, the line centre can typically be located with a minimum statistical uncertainty of ± 0.10 pixels. More details, including examples of typical raw data and fits, have been presented by various authors (Lempert *et al* 1995, Lempert 2000, Hill and Klewicki 1996, Harris 1999).

As illustrated in the previous droplet example, when images are viewed through curved surfaces or interfaces, the effects of refraction can significantly alter the observed displacement. To correct for this, a simple pinhole optical model was employed (Harris *et al* 1996, Harris 1999). The basic idea is to computationally ‘transfer’ the intensity observed at the CCD image plane back to the original fluid object plane. Each pixel in the image plane is mapped onto a ray using a calibrated lens model. This ray is computationally propagated through a model of the experiment until an optical surface is reached. A three-dimensional refraction angle

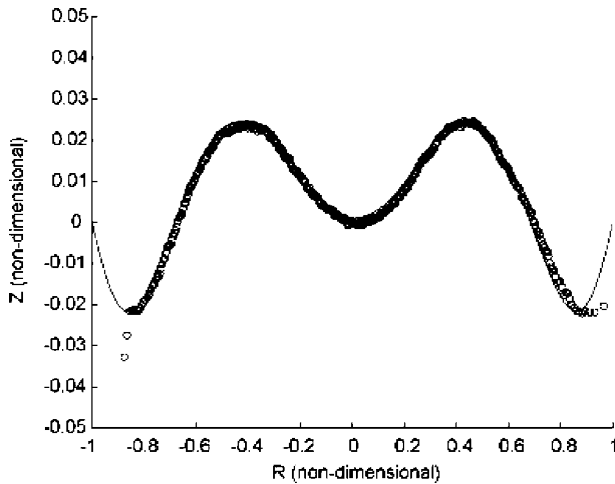


Figure 8. A Lagrangian frame comparison between ray traced data of figure 7 (—) and a numerical computation (○).

is then calculated using Snell’s law. Linear translation is continued until the ‘object’ plane is intersected. If only a single camera is available, then it is assumed that the object plane is the centre of the interrogation sheet. This implies that the line was tagged in the centre of the sheet and that the out-of-plane motion is negligible. If two, stereoscopic, images are available, as is the case for the data of figure 6, (a bottom view, not shown, was also obtained), then the object plane is located at the intersection of the rays corresponding to these two views, which are ray traced simultaneously. Complete details of the procedure, including bench mark tests, can be found in Harris (1999). Figure 7 shows the results of applying the ray tracing procedure to the data from figure 6. Since the curved surface is a cylinder, the principal effect is to distort the radial axis, particularly in the region near the wall.

Figure 8 shows a comparison of the corrected measured displacement data with the displacement obtained by simulating the motion of a tagged line in a velocity field obtained by solving the axisymmetrical Navier–Stokes equations. This code used to obtain the flow field is very similar to one described by Lopez (1990). In figure 8, both axes have been non-dimensionalized to the cylinder radius, R , and it can be seen that, with the exception of the region very near the wall, the agreement is extremely good. It is believed that the discrepancy near the wall is entirely due to errors associated with ray tracing. More detailed examination (Harris 1999) shows that the average deviation between measured and computed displacement is approximately $0.0014R$.

4.5. Results for the unsteady regime

Figure 9 shows seven consecutive images of azimuthal motion (in the r – θ plane) obtained from the bottom camera at four different Reynolds numbers ranging from 5×10^3 to 10^5 . Although it is not readily apparent from figure 9, even at the lowest Reynolds number of 5×10^3 the flow has developed significant unsteadiness. (This is much more apparent when image sequences are displayed in rapid succession on a screen.) There are, however, no discernible small scale features. At a Reynolds number of 10^4 (figure 9(b)) the

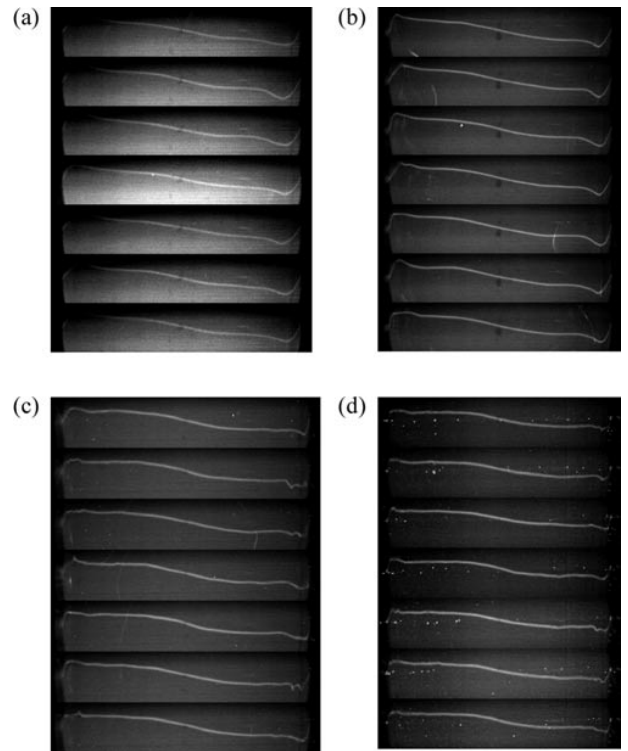


Figure 9. Seven consecutive images of azimuthal motion (in the r – θ plane) of a line tagged into lid driven cylinder flow at four different Reynolds numbers. $Re = 5 \times 10^3$ (a), 10^4 (b), 5×10^4 (c) and 10^5 (d).

magnitude of large scale unsteadiness has increased and small scale features are beginning to evolve near the walls. At $Re = 5 \times 10^4$ (figure 9(c)), small scale features are quite evident. At $Re = 10^5$ (figure 9(d)), the scales of the fine structure are approaching the width of the tagged fluid element. It should be noted that the increased noise in figure 9(d) is a result of scattering from small air bubbles aspirated into the flow from above the rotating end wall. Measurements at the highest Reynolds numbers employed a time delay between tagging and interrogation of less than the $1/60$ s video framing interval. In this case, scattering from the small bubbles by the tagging laser pulse is superimposed on the interrogation image, despite the use of the coloured glass filter. These bubbles were produced only when the apparatus was run at its highest Reynolds number setting and do not appear to be significant enough to perturb the flow.

The two-point turbulent displacement correlation function, $C(r_i, r_j)$, provides a convenient way to present quantitative information about the structure of this flow. The correlation function is defined as

$$C(r_i, r_j) = \frac{\overline{x(r_i)x(r_j)}}{[\overline{x(r_i)^2x(r_j)^2}]^{1/2}} \quad (2)$$

where $x(r_i)$ is the displacement at the i th radial coordinate and the overbars indicate an ensemble average over the individual images obtained for each flow condition (150 frames at Reynolds number 10^4 , ≈ 200 for Reynolds numbers 5×10^4 and 10^5). As the time delay between the tagging and interrogation steps approaches zero, the value of $C(r_i, r_j)$

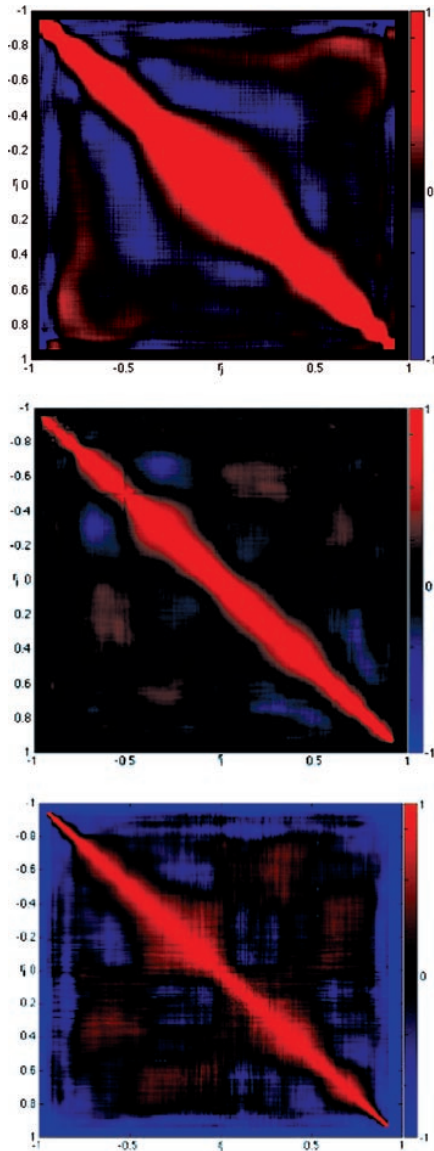


Figure 10. Spatial correlation plots obtained from ensembles of instantaneous images similar to those of figure 9. At $Re = 10^4$ (top), 5×10^4 (middle) and 10^5 (bottom). Red = correlation of 1.0, blue = correlation of -1.0 .

approaches that of the familiar two-point turbulent velocity correlation. Figure 10 shows colour plots of the correlation function of the azimuthal displacement as a function of the non-dimensionalized radial coordinate at three Reynolds numbers. The red diagonal bands are a result of the strongly correlated motion of nearby points. The perfect reflection symmetry across the diagonal band is due to the property of the correlation function $C(r_i, r_j) = C(r_j, r_i)$. The weaker symmetry, $C(r_i, r_j) = C(-r_i, -r_j)$ is an indication of the axisymmetry of the flow itself. The top plot of figure 10 corresponds to a Reynolds number of 10^4 . Of particular interest are the question-mark-shaped features in the upper right-hand and bottom left-hand corners, indicating that the turbulent fluctuations on opposite sides of the cylinder are correlated and in phase. At $Re = 5 \times 10^4$ (middle image), the width of the strongly

correlated diagonal is decreased, indicating a decrease in the characteristic turbulent length scale. There are also multiple off-diagonal features, indicating that the flow is developing some rather complicated large scale structure. The bottom plot of figure 10 corresponds to a Reynolds number of 10^5 and exhibits regions of significant positive and negative correlation. Negative values correspond to turbulent fluctuations which are correlated, but are 180° out of phase. For example, negative correlation at points such as $(r_i = -0.25, r_j = 0.25)$ indicate that, at this Reynolds number, the motions of structures on opposite sides of the core are coupled together in such a way as to produce out-of-phase displacement.

5. Conclusions

Caged dye flow tagging velocimetry has been applied to a wide variety of flow problems, spanning a large range in characteristic length and time scales. Quantitative velocity data for microchannel flow, free falling and electrohydrodynamic droplets and rotating flows spanning a Reynolds number range from of order 0.10 to of order 10^5 have been reported. Visualizations of the highly vortical sublayer flow produced by an evaporating droplet spreading over a surface have also been reported, as has a novel approach for measuring scalar mixing in turbulent pipe flow.

As a more detailed example, caged dye flow tagging has been used to study the complex flow produced in a cylinder with a single rotating end wall. At low Reynolds number (of order 100–2000), visualizations in the r - z plane are in agreement with the dye studies of Escudier. Simultaneous stereoscopic images in the r - z and r - θ planes have been obtained under these conditions. After removal of geometrical distortion produced by the curved walls of the container, quantitative agreement between the experimental images and those predicted using a numerical flow solver is found. At still higher Reynolds number (5×10^3 to 10^5), the flow develops considerable smaller scale, turbulent three-dimensional structure, particularly in the boundary layer on the cylinder walls. Sets of images have been obtained and used to determine statistical quantities such as the spatial correlation function.

Acknowledgments

The authors wish to acknowledge Professors Richard Miles and Garry Brown of Princeton University for their participation in much of the work presented here. Many insightful discussions with Professor John M Lopez of Arizona State University are also acknowledged, as is the technical support of Mr Philip Howard. The work was supported by Molecular Probes, Inc, NASA and the National Science Foundation of the USA.

References

- Barker P, Bishop A and Rubinsztein-Dunlop H 1997 *Appl. Phys. B* **62** 3369

- Bevington P R 1969 *Data Reduction and Error Analysis for the Physical Sciences* (New York: McGraw-Hill)
- Biage M, Harris S R, Lempert W R and Smits A J 1996 *8th Int. Symp. on Applications of Laser Techniques to Fluid Mechanics, Lisbon*
- Boedeker L R 1989 *Opt. Lett.* **14** 473–5
- Brown G L and Lopez J M 1990 *J. Fluid Mech.* **221** 553–76
- Dahm W J A and Dimotakis P E 1990 *J. Fluid Mech.* **217** 299–330
- Dahm W J, Su L K and Southerland K B 1992 *Phys. Fluids* **4** 2191–206
- Dussaud A, Troian S M and Harris S R 1998 *Phys. Fluids* **10** 1588–96
- Escudier M P 1984 *Exp. Fluids* **2** 189–96
- Falco R E and Nocera D 1993 *Particulate Two-Phase Flow* ed M C Rocco (Boston: Butterworth-Heinemann) pp 59–126
- Gendrich C P and Koochesfahani M M 1996 *Exp. Fluids* **22** 67–77
- Gendrich C P, Koochesfahani M M and Nocera D G 1997 *Exp. Fluids* **23** 361–72
- Goss L P, Chen T H, Trump D D, Sarka B and Nejad A S 1991 AIAA-91-0355
- Guilke J E, Gee K R, McMurty P A and Klewicki J C 1996 *Exp. Fluids* **21** 237–42
- Harris S R 1999 *PhD Thesis* Princeton University
- Harris S R, Lempert W R, Hersh L, Burcham C L, Saville D A, Miles R B, Gee K and Haughland R P 1996 *AIAA J.* **34** 449–54
- Hill R B and Klewicki J C 1996 *Exp. Fluids* **20** 142–52
- Kerstein A R and McMurty P M 1994 *Phys. Rev. E* **50** 2057–63
- Koochesfahani M M, Cohn R K, Gendrich C P and Nocera D G 1996 *8th Int. Symp. on Applications of Laser Techniques to Fluid Mechanics, Lisbon*
- Koochesfahani M M and Dimotakis P E 1985 *AIAA J.* **23** 1700–7
- 1986 *J. Fluid Mech.* **170** 83–112
- Lempert W R 2000 *Flow Visualization: Techniques and Examples* ed A J Smits and T T Lim (London: Imperial College Press)
- Lempert W R, Lee D, Harris S R, Miles R B and Gee K 1998 *36th AIAA Aerospace Sciences Meeting, Reno, NV*
- Lempert W R, Magee K, Ronney P, Gee K R and Haughland R P 1995 *Exp. Fluids* **18** 249–57
- Lopez J M 1990 *J. Fluid Mech.* **221** 533–52
- McDaniel J 1983 *Opt. Lett.* **8** 51–3
- Miles R B, Connors J J, Markovitz E C, Howard P J and Roth G J 1989 *Exp. Fluids* **8** 17
- Noullez A, Wallace G, Lempert W, Miles R B and Frisch U 1997 *J. Fluid Mech.* **339** 287–307
- Paul P H, Lee M P and Hanson R K 1989 *Opt. Lett.* **14** 417
- Paul P H, Garguilo M G and Rakestraw D J 1998 *Anal. Chem.* **70** 2459–67
- Popovich A T and Hummel R L 1967 *Chem. Eng. Sci.* **29** 308–12
- Ribarov A R, Wehrmeyer J A, Batliwala F, Pitz R W and DeBarber P H 1999 *AIAA J.* **37** 708–14
- Vizka O and Saville D A 1992 *J. Fluid Mech.* **238** 1–21
- Vogel H U 1975 *Rückströmungsblasen in Drallströmungen. Festschrift 50 Jahr Max-Planck-Institut für Strömungsforschung 1925–1975*
- Zhang J and Melton L A 1994 *Appl. Opt.* **33** 192–200
- Zimmermann M and Miles R B 1980 *Appl. Phys. Lett.* **37** 885